Vegetation Products Derived from *Fengyun-3D* Medium Resolution Spectral Imager-II

Xiuzhen HAN, Jun YANG*, Shihao TANG, and Yang HAN

National Satellite Meteorological Center, China Meteorological Administration, Beijing 100081

(Received February 15, 2020; in final form April 2, 2020)

ABSTRACT

The surface vegetation condition has been operationally monitored from space for many years by the Advanced Very High Resolution Radiometer (AVHRR) and the Moderate Resolution Imaging Spectroradiometer (MODIS) instruments. As these instruments are close to the end of their design life, the surface vegetation products are required by many users from the new satellite missions. The MEdium Resolution Spectral Imager-II (MERSI-II) onboard the Fengyun (FY) satellite (FY-3 series; *FY-3D*) is used to retrieve surface vegetation parameters. First, MERSI-II solar channel measurements at the red and near-infrared (NIR) bands at the top of atmosphere (TOA) are corrected to the surface reflectances at the top of canopy (TOC) by removing the contributions of scattering and absorption of molecules and aerosols. The normalized difference vegetation index (NDVI) at both the TOA and TOC is then produced by using the same algorithms as the MODIS and AVHRR. The MERSI-II enhanced VI (EVI) at the TOC is also developed. The MODIS technique of compositing the NDVI at various timescales is applied to MERSI-II to generate the gridded products at different resolutions. The MERSI-II VI products are consistent with the MODIS data without systematic biases. Compared to the current MERSI-II EVI generated from the ground operational system, the MERSI-II EVI from this study has a much better agreement with MODIS after atmospheric correction.

Key words: MEdium Resolution Spectral Imager-II (MERSI-II), Fengyun (FY) satellite, vegetation index (VI), atmospheric correction

Citation: Han, X. Z., J. Yang, S. H. Tang, et al., 2020: Vegetation products derived from *Fengyun-3D* Medium Resolution Spectral Imager-II. *J. Meteor. Res.*, **34**(4), 775–785, doi: 10.1007/s13351-020-0027-5.

1. Introduction

The satellite vegetation index (VI) products derived from the Advanced Very High Resolution Radiometer (AVHRR) on board the NOAA satellites and NASA Moderate Resolution Imaging Spectroradiometer (MODIS) have provided consistent spatial and temporal comparisons of global vegetation conditions. Gridded VI maps depicting spatial and temporal variations in vegetation activity are derived at 16-day and monthly intervals for precise seasonal and interannual monitoring of the earth's vegetation. Vegetation indices, such as normalized difference VI (NDVI), enhanced VI (EVI), and green vegetation fraction (GVF), are widely used to measure the canopy or vegetation variables. NDVI, originally developed by Rouse et al. (1973), was used to quantitatively assess the biophysics characteristics of the Great Plains of North America. In addition, it is defined by the ratio of the difference of red and infrared radiances over their sum and ranges within [−1, 1], and can be applied to monitor the drought and verify climate simulation (Zeng et al., 2000). In addition, the annual NDVI datasets can be used to classify the vegetation or land type. The well-known International Geosphere–Biosphere Programme (IGBP) product is based on NDVI values from the MODIS sensor and is now a popular and useful database.

For assessing the canopy structural variations more efficiently, EVI was developed to strengthen the signal from vegetation by adopting the blue radiance, specifically to make it sensitive in high biomass regions, to degrade the response from vegetation and background and to reduce the impact of molecule scattering and aerosol

Supported by the National Key Research and Development Program of China (2018YFC1506500).

*Corresponding author: junyang@cma.gov.cn.

contaminations in the atmosphere (Huete et al., 1999). Different from NDVI, EVI is based on the top of canopy (TOC) radiances at red, blue, and near-infrared (NIR) bands, which reduce the atmospheric molecular scattering and aerosol influences above the TOC. It can optimize the signal from the vegetation to reflect their distributions and variations.

After the AVHRR and the MODIS instruments, the MEdium Resolution Spectral Imager (MERSI) have been carried on board Fengyun-3 (FY-3) series of satellites. While the MERSI-I on *FY-3C* has fewer channels than the MERSI-II on *FY-3D*, both can be used for monitoring surface vegetations. Compared with NASA MODIS and NOAA Visible Infrared Imaging Radiometer Suite (VIIRS), MERSI-II has 25 channels in total and has more solar bands for more environmental applications. Many of the MERSI-II channels are in common to the MODIS and the VIIRS, and thus can produce the same quality of surface products if the same algorithms can be developed and applied for retrievals. The primary purpose of this study is to develop the vegetation algorithm for MERSI and to demonstrate the quality of the VI products. In next section, we first illustrate the MERSI-II responses at visible to NIR to atmospheric and surface parameters. This understanding is required for developing the scheme of atmospheric correction. In Section 3, the MERSI-II datasets are discussed as inputs to the surface VI algorithm. Section 4 presents the theoretical description of VI algorithms. Section 5 shows the EVI products derived from the MERSI-II measurements and their comparison with MODIS parameters. Summary and conclusions will be presented in the last section.

2. Responses of satellite reflectance to surface properties

To understand the responses of satellite reflectance to surface parameters, we utilize the Unified Non-Linear (UNL) Vector Radiative Transfer Model (VRTM; Wang et al., 2014) to simulate the atmospheric scattering and absorption from molecules and aerosols. UNL-VRTM is designed for the simulation of atmospheric remote sensing observations and for the inversion of aerosol, gas, cloud, and/or surface properties from these observations. It comprises a vector linearized discrete ordinate radiative transfer (VLIDORT) for radiative transfer, a linearized Mie and T-matrix code for aerosol single scattering, a Rayleigh scattering module, and line-by-line absorption computation with HITRAN (high resolution transmission) database. VLIDORT is a linearized vector radiative transfer solver and it can output full stokes vectors and their Jacobians with respect to physical and optical parameter of clouds and/or aerosols. The T-matrix method, formally introduced by Waterman (1965), was incorporated as a vital component in UNL-VRTM. It is the fastest exact technique for the computation of non-spherical scattering based on a direct solution of Maxwell's equations, which will provide better solutions for aerosol scattering. The UNL-VRTM in principle simulates the radiative transfer from ultraviolet to infrared wavelengths.

Figure 1 shows the simulated top of atmosphere (TOA) reflectance at various sun and sensor viewing angles, and the relative azimuthal angle between sun and sensor, respectively. In this case, land surface emissivity is set to zero. The TOA reflectance is computed by inputting midlatitude summer atmospheric profile into the model. The variations of the reflectance with respect to the wavelength are also shown. In Fig. 1a, a strong relationship between the molecular scattering and the wavelength is identified. Clearly, the atmospheric contribution from molecular scattering is strongly wavelength dependent. This is because the molecular scattering is in the Rayleigh scattering regime and the scattering intensity is inversely proportional to the wavelength of the 4th power ($\sim 1/\lambda^{-4}$).

Figure 1b illustrates the effect of the aerosol scattering and absorption. Two aerosol refractive indices of 1.53 + 0.008i and 1.75 + 0.43i are selected. The first one represents the more scattering type and the second stands for an absorbing type. Moreover, the aerosol optical depth is set to 1 for this case, and the other parameters are the same as those in Fig. 1a. The simulations from UNL-VRTM show that the absorbing aerosol resulted in lower TOA reflectivity than scattering aerosol and the reflectance at TOA becomes less wavelength dependent.

Surface albedo is another parameter that affects the radiative transfer. Direct solar and diffuse radiation to the ground can be reflected by the surface, and then these reflected radiation travel through the atmosphere. Without knowledge of the interaction between surface and atmosphere, the properties of both atmosphere and surface cannot be accurately separated. Figure 1c shows the distribution of reflectance when setting the albedo to 0, 0.2, and 0.5, respectively. Overall, the reflectance at TOA is highly modulated by the surface albedo. The contributions from absorption and scattering from atmospheric molecules and aerosols, and surface albedo, result in a complex relationship between TOA reflectivity and surface albedo. To accurately simulate the TOA reflectance under cloud-free atmospheres, we need to include the scattering and absorption processes from gaseous molecules and aerosols. On the other hand, to accurately infer the surface properties from the TOA measurements at

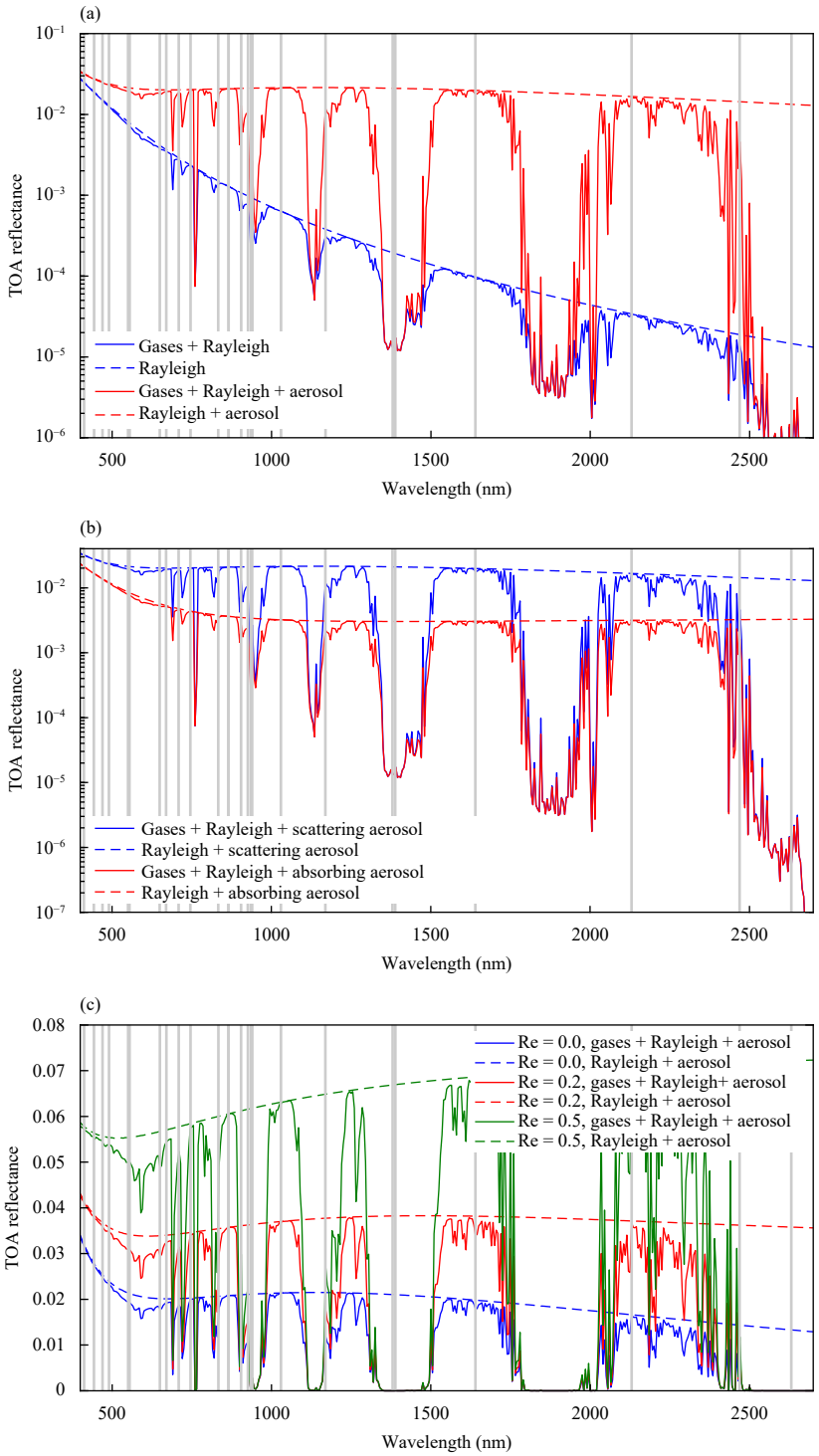

Fig. 1. Distributions of TOA reflectance with respect to wavelength (nm) calculated by UNL-VRTM using the midlatitude summer atmospheric profile. The solar zenith angle, view zenith angle, and relative azimuth angle are 60°, 30°, and 0°, respectively. (a) The surface albedo is set to 0, aerosol optical depth is set to 1, and the aerosol is assumed to be non-absorbing; (b) as in Fig. 1a, but for absorbing aerosol; and (c) as in Fig. 1b, but the surface albedo is set to 0, 0.2, and 0.5.

MERSI-II reflective bands, we also need to make the atmospheric molecular correction and improve the derivation of VI effectively. This correction scheme will be discussed in Section 4.

3. MERSI-II datasets

On 14 November 2017, China Meteorological Administration (CMA) launched *FY-3D* satellite (fourth of the

Fengyun-3 series) to the altitude of 836 km. *FY-3D* is configured in an afternoon orbit at equatorial crossing time (ECT) of 1400 local time. Today, a suite of products has been developed from 11 instruments on *FY-3D* for weather and environmental monitoring, and data assimilation. The MERSI-II is one of the most important payloads and has capabilities similar to or better than the MODIS and the VIIRS, and provided more than 20 environmental parameters. It provides the observations at 25 visible and infrared bands (see Han et al., 2019). Among them, six-channel data are made at a 250-m resolution and bands 1–4 are primarily used for ecological and environmental applications. The MERSI-II instrument is well calibrated (Xu et al., 2018) and its L1 data have been released to the world-wide communities for operational uses. The true color composite imagery is often made by red (0.68 μm), green (0.55 μm), and blue (0.47 μm) bands of MERSI-II data to reflect the nature scenes (Han et al., 2019). Moreover, the red (0.65 μm) and NIR (0.865 μm) bands can be utilized to derive NDVI and EVI at their spatial resolution of 250 m.

The MERSI-II L1 datasets are released in the Hierarchy Data Format (HDF), which can be decoded by using many open-source codes. An example of file naming convention for MERSI-II L1 datasets is shown as FY3D_MERSI_GBAL_L1_20190421_0000_1000M_MS.HDF. The naming convention includes spacecraft ID, instrument ID, domain description, data level, data start date, data start time, spatial resolution, storage unit, and extension. The MERSI-II operational data are generated as a 5-min granule at resolutions of 250 m and 1 km in HDF. One-granule file usually contains 2000 scanlines and 2048 field of views (FOVs). The products also include earth view science data for emissive and reflective solar bands, geolocation information, and quality flag (QF). For the earth view science data, they contain both the digital numbers and their calibration coefficients for both emissive and reflective solar bands. There are variations of latitude, longitude, land sea mask, land cover, digital elevation model (DEM), sensor zenith, sensor azimuth, solar zenith, and solar azimuth.

4. MERSI-II VI algorithms

Vegetation canopy has a property that reflects less sunlight at the red band and reflects more in the NIR band. Reflected red energy decreases with the plant development due to chlorophyll absorption in photosynthetic leaves. Reflected NIR energy increases with plant development through scattering processes. Thus, it is difficult to relate the reflected energy at each individual wavelength to the vegetation structure and composition. However, the spectral information from red to NIR wavelength is rich for extracting the properties of vegetation structure and composition. The combined PROSPECT leaf optical properties model and SAIL (Scattering by Arbitrary Inclined Leaves) canopy bidirectional reflectance model, also referred to as PROSAIL, have been used for many years to study plant canopy spectral and directional reflectance in the solar domain. Figure 2 shows the vegetation reflectance spectrum simulated by using the PROSAIL model (Jacquemoud et al., 2000). In PROSAIL leaf optical model, a total of 15 parameters including leaf structure, leaf area index (LAI), contents of chlorophyll, brown pigment, water and dry matter, and refractive index are essential for computing the leave optical thickness. In addition, PROSAIL also requires solar zenith and sensor viewing angles, and solar and sensor azimuthal angles in simulation. Note that the reflectances at the wavelength less than 0.7 μm are low due to the strong absorption of leaf chlorophyll. From the wavelength greater than 0.8 μm, the reflectance increases sharply. The reflectance difference between the two wavelengths formulates the foundation for remote sensing of vegetation.

In this study, the MERSI-II bands at 0.47, 0.65, and 0.87 μm are selected for VI calculations. First, MERSI-II data are checked for clear conditions with a cloud mask algorithm. Then, three bands are corrected for removing the atmospheric contributions from molecular and aerosol scattering and absorption. After that, VIs are computed at all clear pixels in orbital granular data and then gridded to the equal latitude and longitude files for producing a composite dataset within a week to a month. The entire flow chart is shown in Fig. 3 and each component is discussed in the following section.

4.1 *Cloud mask*

Cloud detection is an eternal topic for remote sensing.

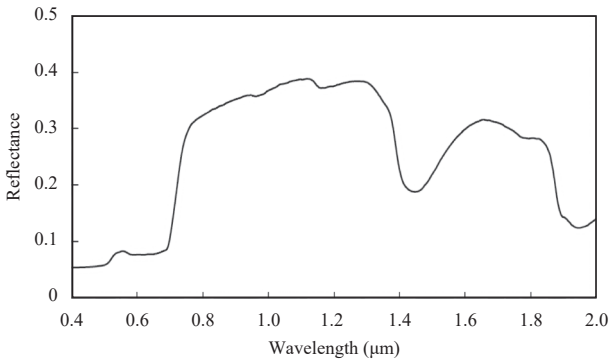

Fig. 2. Reflected energy from vegetation and grass at wavelength from 0.4 to 2.0 μm.

When the sky is clear, the effect of the absorption and scattering from atmospheric molecule and aerosol needs to be removed. If there exist clouds over the surface, the signals from the surface for red bands will be blocked. Therefore, cloud mask is a pre-requisite for the derivation of VI. An improved cloud detection scheme was developed for AVHRR data (Saunders and Kriebel, 1988; Stroppiana et al., 2000). It can detect the pixels as cloud free, cloud filled, or partly cloudy. In this study, the cloud detection algorithm is employed for MERSI-II to identify the pixels with clear/cloudy conditions (Fig. 4). The algorithm is based on the observations (reflectance or brightness temperature) of channels with the center wavelength at 0.65, 0.865, and 12 μm. A pixel will be classified as a cloud through three tests:

$$\begin{aligned}&(\rho_{\rm red}^{\rm TOA}+\rho_{\rm NIR}^{\rm TOA}>1.2)|(T_{\rm B}^{12\mu{\rm m}}<265{\rm K})|\\&(\rho_{\rm red}^{\rm TOA}+\rho_{\rm NIR}^{\rm TOA}>0.8\&T_{\rm B}^{12\mu{\rm m}}<285{\rm K}),\end{aligned}\tag{1}$$

where $\rho_{\rm red}^{\rm TOA}$, $\rho_{\rm NIR}^{\rm TOA}$, and $T_{\rm B}^{12\mu{\rm m}}$ are the TOA reflectance at red and NIR bands, and brightness temperature of the channel with center wavelength at 12 μm, respectively. In other words, a pixel will be determined to be cloudy if the sum of reflectance from red and NIR channels is larger than 120%, or its brightness temperature is less than 265 K, or the sum of reflectance is larger than 0.8 and its brightness temperature is less than 285 K.

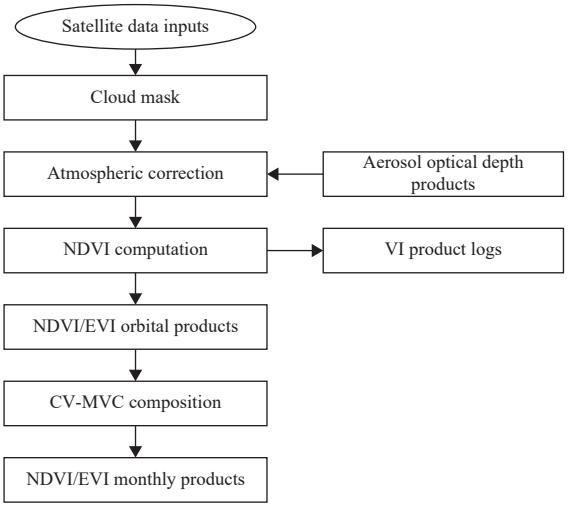

Fig. 3. Flow chart of MERSI-II VI system.

4.2 *Atmospheric correction*

Atmospheric correction is an essential step in deriving VIs from the MERSI-II. Gaseous and aerosol's absorption and scattering can interfere the radiance from the earth to the satellite. Absorption will reduce the radiation intensity in a haziness effect while scattering redirects the electromagnetic energy in the atmosphere causing an adjacent effect to the neighborhood pixels. In previous studies, many effective methods were developed for removing the absorption and scattering effects from the atmosphere to obtain true surface reflectance. Today, the common method for atmospheric correction is based on the radiative transfer model developed by Vermote et al. (1997), i.e., the 6S model, which is briefly summarized as follows.

Assuming that the surface is uniform Lambertian type, the TOA reflectance can be described by:

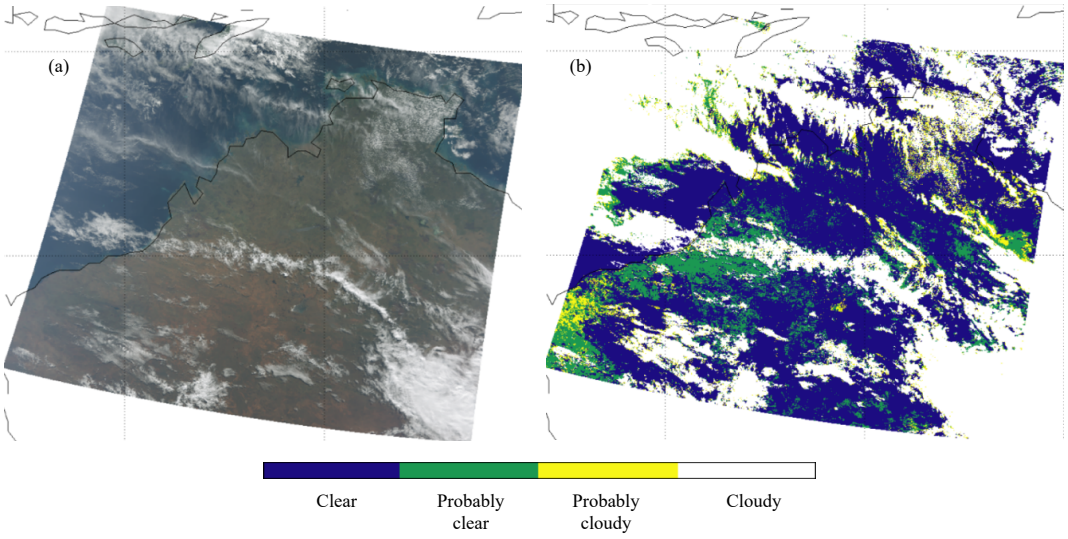

Fig. 4. (a) *FY-3D* MERSI true color composite imagery and (b) the distribution of cloud detection. The blue, green, yellow, and white colors represent the conditions of clear, probably clear, probably cloudy, and cloudy, respectively.

$$\rho^{\mathrm{TOA}}(\theta_{\mathrm{s}},\theta_{\mathrm{v}},\varphi,p,\mathrm{AOD},U_{\mathrm{H_2O}},U_{\mathrm{O_3}}) = T_{\mathrm{OG}}(m,p)T_{\mathrm{O_3}}(m,U_{\mathrm{O_3}})[\rho_{\mathrm{atm}}(\theta_{\mathrm{s}},\theta_{\mathrm{v}},\varphi,p,\mathrm{AOD},U_{\mathrm{H_2O}}) + T_{\mathrm{atm}}(\theta_{\mathrm{s}},\theta_{\mathrm{v}},p,\mathrm{AOD})\frac{\rho_{\mathrm{s}}}{1-S_{\mathrm{atm}}(p,\mathrm{AOD})\rho_{\mathrm{s}}}T_{\mathrm{H_2O}}(m,U_{\mathrm{O_3}})], \quad (2)$$

where θ_{s}, θ_{v}, φ, p, AOD, $U_{\mathrm{H_2O}}$, and $U_{\mathrm{O_3}}$ are the solar zenith angle, view zenith angle, the difference between solar azimuth and view azimuth angle, pressure, aerosol model optical properties, integrated water vapor content, and integrated columnar ozone content; ρ^{TOA}, ρ_{atm}, and ρ_{s} are the reflectance from the TOA, atmospheric intrinsic, and surface, respectively; $T_{\mathrm{O_3}}$, $T_{\mathrm{H_2O}}$, and T_{OG} are the atmospheric transmittance of ozone, water vapor, and other gases, respectively; and m is air mass along inclined path and S_{atm} is the atmospheric spherical albedo, a function of AOD and p. For detailed information please refer to Han et al. (2019). The atmospheric intrinsic reflectance is relevant to the molecular (Rayleigh) scattering and aerosol scattering.

A comprehensive look-up table (LUT) should be created to perform the atmospheric correction with a high computation efficiency and accuracy. In this study, the inputs of LUT consist of 8 continental absorbing aerosol with optical depths of 0.05, 0.1, 0.2, 0.4, 0.8, 1.2, 1.6, and 2.0, 13 solar zenith angles ranging from 0 to 80° with interval of 6°, 13 view zenith angles ranging from 0 to 80° with interval of 6°, and 11 relative azimuth angles from 0 to 180° with interval of 18°. In addition, the outputs include transmittance of molecule, ozone, water vapor, upwelling and downwelling radiation, and reflectance of aerosol at TOA. In the algorithm, LUT values are used to obtain the various parameters in Eq. (2) with atmospheric state variables, and actual solar and satellite angles. The US standard atmospheric profiles of temperature, water vapor, and ozone are used in radiative transfer calculations. The AOD concentration at a given location is taken from the MODIS green band. It is planned to replace the MODIS AOD once MERSI-II AOD product becomes operational. Finally, the corrected surface reflectance can be accurately computed from Eq. (1). Figure 5 shows a flow chart for atmospheric correction, following the steps below:

(1) Read in the MERSI-II L1 data, land/water mask, and examine each pixel if it is a land or water pixel;

(2) Check if it is a cloudy pixel. For a cloudy pixel, skip to step 5;

(3) Use sun and satellite viewing angles, sun and satellite relative azimuthal angles, and AOD to obtain the atmospheric correction coefficients through interpolations with the LUT data;

(4) Compute the surface reflectance with the atmospheric correction parameters;

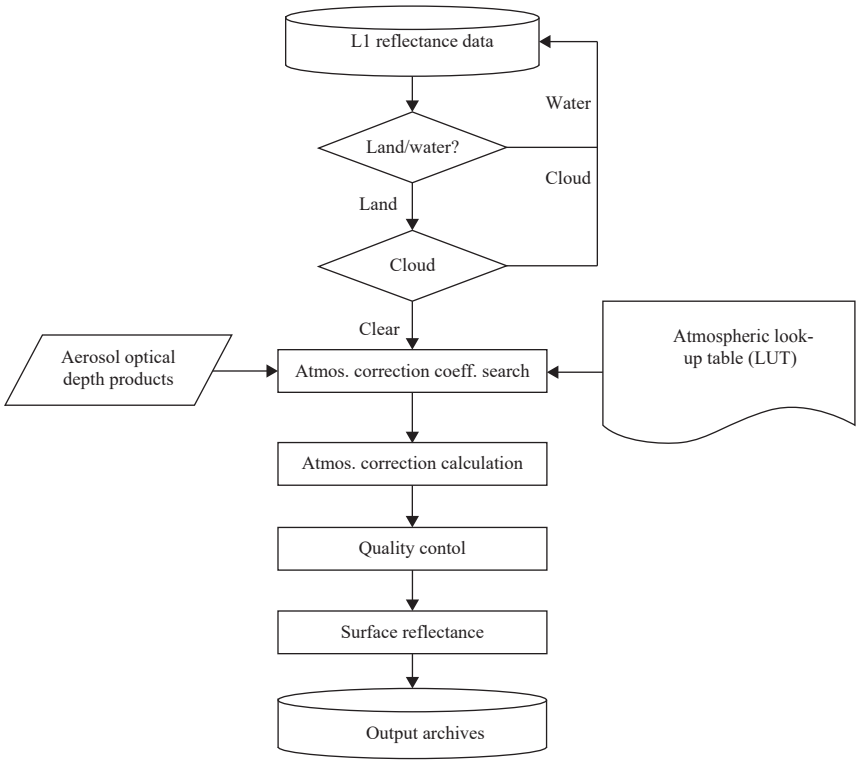

Fig. 5. Flow chart for MERSI-II atmospheric correction to produce the reflectance at surface.

(5) Add quality control flag;

(6) Output the surface reflectance (blue, red, and NIR), NDVI, EVI, and QFs at each pixel.

Figure 6 compares the true color composite images produced from a monthly MERSI-II red, green, and blue band data before and after atmospheric correction. It is easily seen that a layer of milky-white fog is removed after atmospheric correction. The texture and gray information of dark targets can be better detected, compared with the scene before atmospheric correction.

4.3 *VI calculations*

Vegetation indices are important parameters to monitor the photo-synthesis processes and structural characteristics of surface canopy. Since VIs are intrinsic physical quantities, they are widely used for assessing many biophysical and biochemical variables, including canopy chlorophyll content (Blackburn, 1998), LAI, GVF (Baret et al., 1995; Gutman and Ignatov, 1998), gross primary productivity (GPP; Sims et al., 2006), and fraction of photosynthetically active radiation (FAPAR) absorbed by the vegetation (Myneni et al., 1997a, b).

The NDVI is defined by the ratio of the combination of the reflectance of red and NIR bands and the difference of them:

$$\mathrm{NDVI} = \frac{\rho_{\mathrm{NIR}} - \rho_{\mathrm{red}}}{\rho_{\mathrm{NIR}} + \rho_{\mathrm{red}}}, \tag{3}$$

where ρ_{NIR} and ρ_{red} are the reflectance of the NIR and red bands, respectively and can be either the values at the TOA or ones at the TOC after atmospheric correction. NDVI can be derived at either TOA or TOC, which are referred to as $\mathrm{NDVI}_{\mathrm{TOA}}$ and $\mathrm{NDVI}_{\mathrm{TOC}}$, respectively.

Since NDVI turns saturated easily over the dense vegetation areas, the EVI is proposed by Huete et al. (1999) and is expressed as:

$$\mathrm{EVI}_{\mathrm{TOC}} = \frac{(1+L)\cdot(\rho_{\mathrm{NIR}}^{\mathrm{TOC}} - \rho_{\mathrm{red}}^{\mathrm{TOC}})}{\rho_{\mathrm{NIR}}^{\mathrm{TOC}} + C_{\mathrm{red}}\rho_{\mathrm{red}}^{\mathrm{TOC}} - C_{\mathrm{blue}}\rho_{\mathrm{blue}}^{\mathrm{TOC}} + L}, \tag{4}$$

where $\rho_{\mathrm{NIR}}^{\mathrm{TOC}}$, $\rho_{\mathrm{red}}^{\mathrm{TOC}}$, and $\rho_{\mathrm{blue}}^{\mathrm{TOC}}$ are the TOC reflectance in the NIR, red, and blue bands, respectively. The NIR, red, and blue bands of MERSI-II onboard *FY-3D* satellite locate at 0.865, 0.65, and 0.47 μm. These bands are close to those bands of the MODIS and the VIIRS. Thus, in this study, L, C_{red}, and C_{blue} are set to MODIS and VIIRS values of 1.0, 6.5, and 7.5, respectively.

4.4 *Gridding and compositing*

So far, user communities prefer to have the VI products produced from satellites in gridded format. Thus, the earlier AVHRR, MODIS, and VIIRS processing algorithms all include the gridding and compositing modules to project the VI from the granule to the equal latitude and longitude grids. Various grid resolutions from 0.0025° (250 m) to 0.1° (10 km) can be generated from the data for a period of time (daily rolling weekly, 16 days or monthly). The highest resolution is close to the original sensor pixel resolution at nadir. Take a VIIRS as an example, the entire gridding and compositing process starts with VIIRS TOA and TOC reflectance granule data. The algorithm projects the data using nearest-neighbor method onto a global 0.003° (333-m) grid. This grid is based on the Plate Carrée map projection and consists of 120,000 × 60,000 grid points in the global map, which spans from 90° (north edge) to −90° (south edge) in the latitudinal and from −180° (west) to 180° (east) in the longitudinal directions.

In this study, the MERSI-II daily surface reflectance data in a monthly period are composited to a single file containing NDVI and EVI parameters. The monthly products have a spatial resolution of 0.1°, which is the same as MODIS monthly 0.1° data. To achieve a global

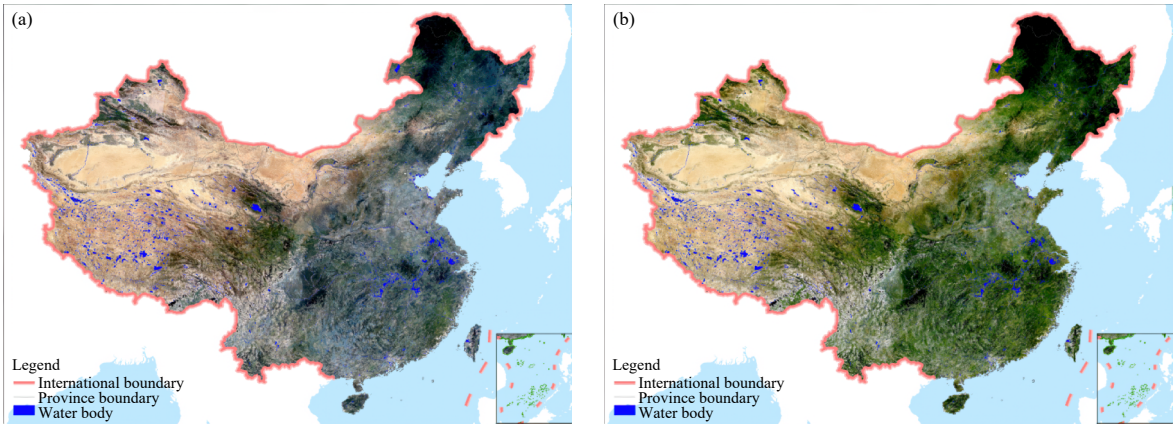

Fig. 6. *FY-3D* MERSI monthly (May 2018) true color composite imagery (a) before and (b) after atmospheric correction.

or local distribution of VIs, constrained view angle-maximum value composite (CV-MVC) approach developed for MODIS is employed to MERSI gridding and compositing (Huete et al., 1999). Instead of using the maximum value of VIs, CV-MVC selects the two highest values of VIs, which are also closest to nadir under the clear condition, and the optimal values are constrained by the zenith angle. If there only exists one cloud-free pixel, it will be selected as the composite data directly. While all data are contaminated by the clouds, the constraint of view angle will be loose to find a proxy value for the grid, and the cloud flags or the quality assurance flags will be also created.

5. Assessment of MERSI-II VI products

The main purpose of developing MERSI-II NDVI and EVI products is to continue AVHRR and MODIS NDVI time series for ecological monitoring and environmental applications. Thus, understanding the quality of the current products with respect to MODIS is of particular importance. For MODIS, NDVI accuracy is claimed to be within ± 0.025, which represents the ability of the 16-day VI products in retrieving the TOC and nadir VI values when observations are of high quality (clear, no sub-pixel cloud, low aerosol, and sensor view angle < 30°). This estimate is based on comparisons with Aerosol Robotic Network (AERONET)-corrected data, other space and airborne sensors, and radiometric field measurements over a range of biomes and seasonality. MODIS EVI is claimed within ± 0.015. Errors in the red band associated with residual atmospheric effects are the main source of the NDVI errors. Thus, a VI consistency check between MERSI-II and MODIS is a first step toward building a robust climate data record.

Figure 7a shows the MERSI-II NDVI products in May 2018, derived from the algorithm without atmospheric correction while Fig. 7b corresponds to the one with atmospheric correction. The data have a spatial resolution of 0.1° latitude × 0.1° longitude. It is clearly demonstrated that the MERSI-II NDVI after atmospheric correction has higher values in central China. This proves the values of atmospheric correction in the algorithm, which can result in better surface VI monitoring. In general, central China has more atmospheric aerosol loading. If its contribution to the TOA reflectance is not removed, surface vegetation information can be significantly obscured and lower NDVI values are likely produced. In the rest of China, the two products have similar patterns due to less aerosol influences.

Figure 8 compares two MERSI-II products with MODIS NDVI at the TOC, in which a total of 90,639 points within the Chinese territory are all used for the comparison. MERSI-II NDVI at the TOA and TOC illustrates the products without and with atmospheric correction, respectively. MODIS NDVI at the TOC is used as "truth" for this comparison. It is shown that the MERSI-II NDVI at the TOC has a higher correlation (~0.89) with MODIS than MERSI-II NDVI at the TOA (~0.84). Moreover, more data points from MERSI-II NDVI at TOC are clustered to the 1 : 1 line. The relationship between MERSI-II and MODIS NDVI at TOC is derived as

$$\mathrm{NDVI_{MERSI}} = 0.0507 + 0.9434 \times \mathrm{NDVI_{MODIS}}. \quad (5)$$

Equation (5) can be also used for converting MODIS and MERSI VI products for generating a long-term NDVI climate data record.

As indicated earlier, in dense vegetation covered land, NDVI can approach very high values or become saturated. Thus, in the current FY satellite ground system, both EVI and NDVI are generated for operational uses. Figure 9 compares the MERSI EVI at the TOC from this

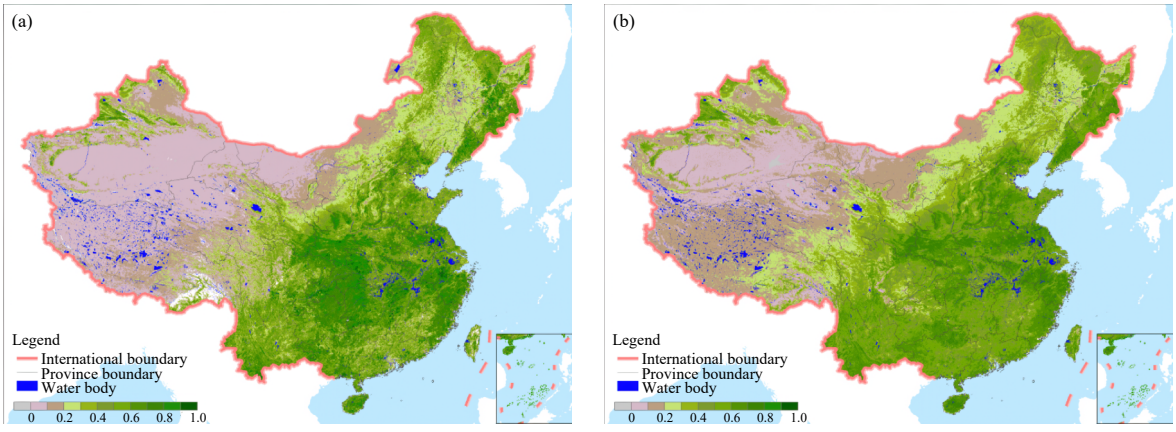

Fig. 7. Monthly composite MERSI-II NDVI (a) before and (b) after atmospheric correction in May 2018.

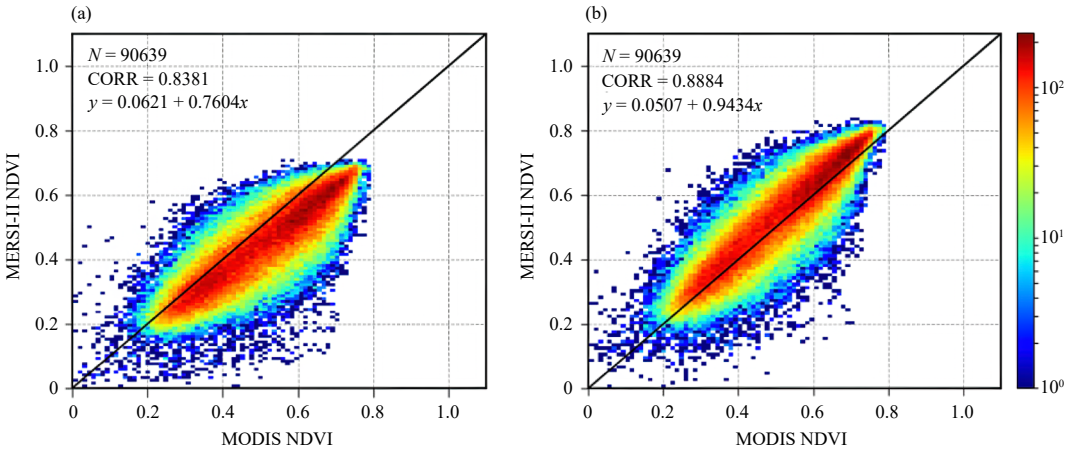

Fig. 8. MERSI-II NDVI against MODIS NDVI in China (a) before and (b) after atmospheric correction in May 2018. The different colors indicate the different numbers of points.

study with the one from the operational system. Apparently, the operational EVI shows much higher values, compared with our retrievals. This requires a further verification of our new EVI products. Figure 10 compares two MERSI EVI products with MODIS EVI. It is clearly seen that the MERSI-II EVI from this study is closer to MODIS EVI, as indicated by its high correlation coefficient and more data points being clustered to the 1 : 1 line. Apparently, the MERSI EVI from the current operational system is not produced correctly. The root cause for this discrepancy requires further studies.

The MERSI-II EVI from this study is also compared with MODIS EVI under various surface conditions, as illustrated in Fig. 11. A land type database (MCD12C1 Version 6) is used to assess the dependence of MERSI-II VI quality on land type. MCD12C1 provides maps of the International Geosphere–Biosphere Programme (IGBP) and LAI classification schemes at yearly intervals at a 0.05° spatial resolution for the entire globe. From the LAI scheme, MCD12C1 produces six classifications: grasses, shrubs, broadleaf crops, savannah, broadleaf forests, and needle leaf forests. Here, the EVIs over grasses, forests, and crops are chosen for comparison. In the forest area, two products have a general consistency in the EVI dynamic range but more scattered data points. Over croplands, the MERSI EVI has the best correlation (0.94) with MODIS EVI, and with the smallest bias.

6. Summary and conclusions

The *FY-3D* satellite was launched on 17 November 2017 with a MERSI-II on board, and the MERSI-II has 25 bands from visible to infrared wavelengths and is well calibrated. It has been performed very well in orbit and provides the user community with a good quality of L1 data. Many environmental data records (EDR) have been produced from MERSI-II, and have been assessed with in situ or other same category of satellite products for understanding the quality. It has been found that the cur-

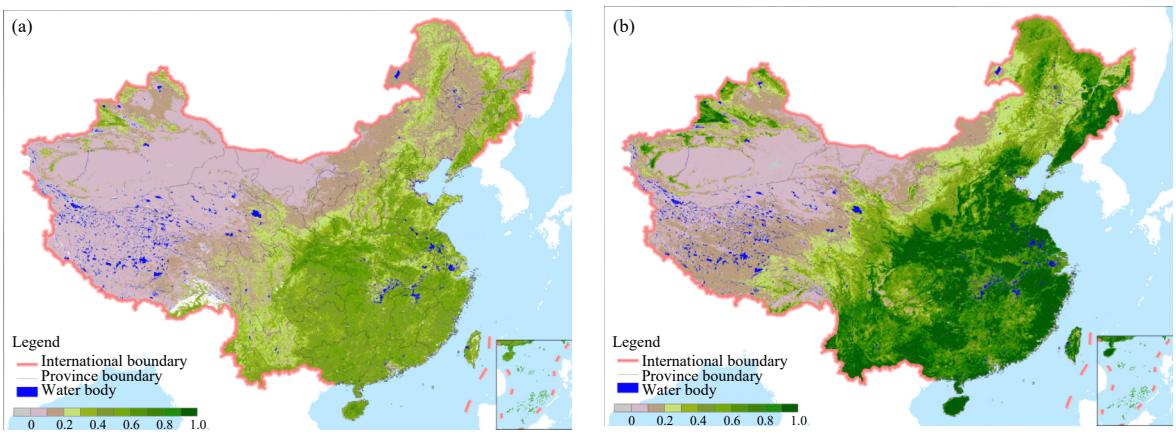

Fig. 9. Monthly composite MERSI-II EVI from (a) this study and (b) the Fengyun operational system in May 2018.

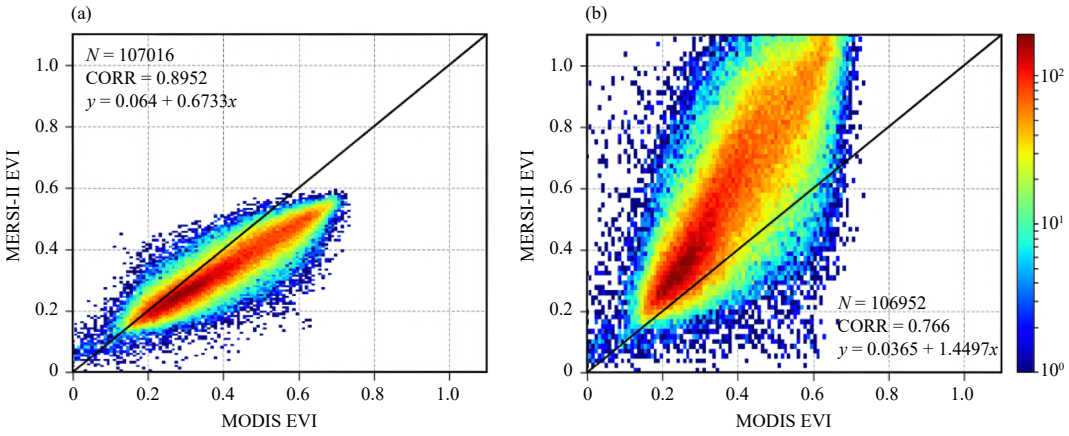

Fig. 10. Comparisons of MERSI-II and MODIS EVI from two processing algorithms: (a) the improved algorithm of this study and (b) the Fengyun ground processing system.

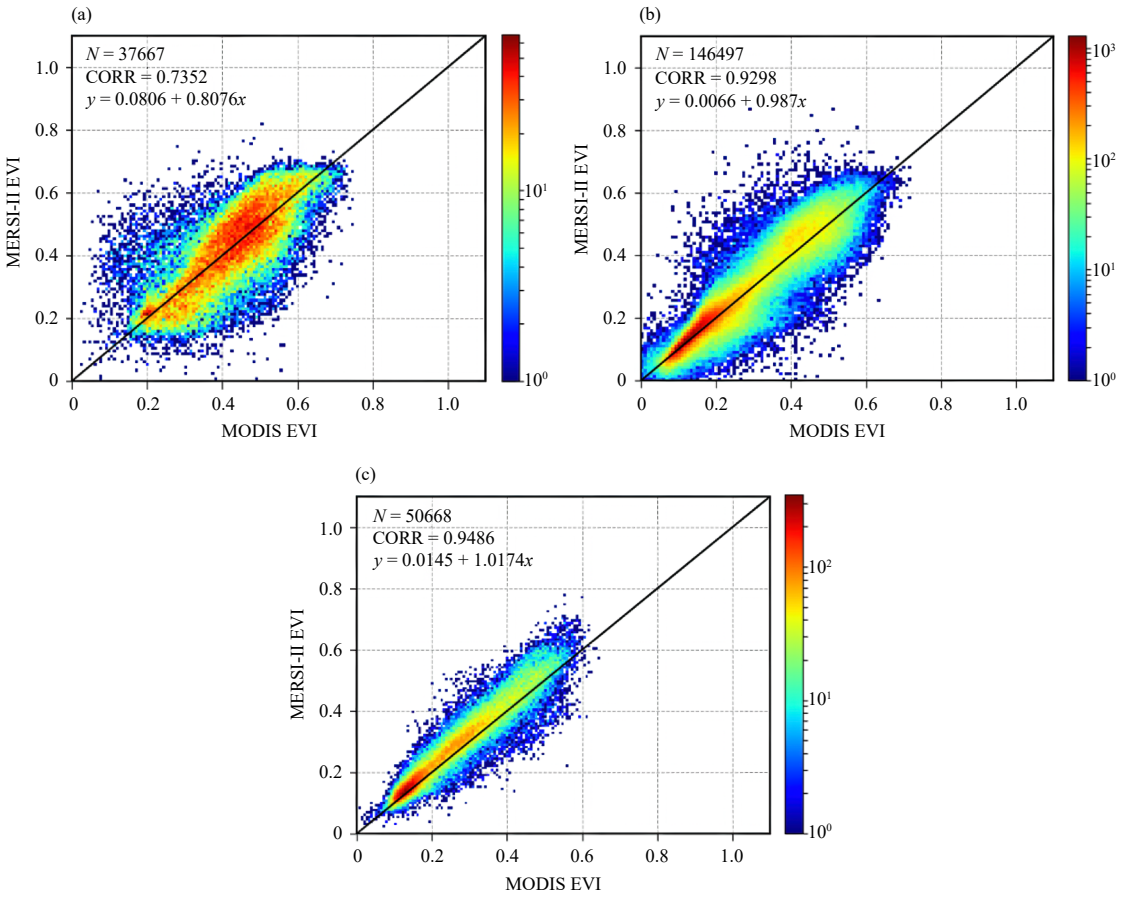

Fig. 11. MERSI-II EVI vs. MODIS EVI for (a) forest, (b) grassland, and (c) croplands in May 2018.

rent MERSI-II EVI products generated from the current FY ground processing system have a large bias, compared to the MODIS product. In order to continue the MODIS VI data records from MERSI-II, we need to develop a new VI algorithm for MERSI-II applications.

In developing MERSI-II VI algorithm, we first utilized the UNL-VRTM to comprehensively simulate the responses of satellite measurements at the TOA to various physical parameters and found that the aerosol scattering and absorption have significant contributions at red and NIR bands, and thus can obscure the surface reflective properties. Therefore, the MERSI-II VI algorithm must include a key component of atmospheric correction. In the atmospheric correction module, the ra-

diative transfer model is based on 6S model that analytically relates the reflectance at the TOA to the optical properties including surface albedo. An LUT is made from 6S and used in the retrieval system for fast computation. Since the aerosol optical depth corresponding to the MERSI-II pixels must be specified, MODIS AOD at 550 μm is collocated with MERSI-II data and used in the algorithm. It is highly recommended that the MERSI-II AOD be developed as part of this system so that the entire MERSI-II EDR products can be produced with a full closure.

Currently, the MERSI-II VI algorithm also requires a high-quality cloud detection algorithm. In this study, we implemented an earlier developed AVHRR cloud algorithm, which works well for most conditions. However, the quality control of MERSI-II VI products still has some room to improve once the MERSI-II cloud products become fully operational. The gridding and compositing of MERSI-II VI products are still in its early phase. More products with different spatial and temporal resolutions are required.

The main purpose of this study is to connect the MERSI-II VI products with MODIS long-term records. Thus, the MERSI-II VI is compared with MODIS in several ways. If MERSI-II reflectances at red and NIR bands are not corrected to the canopy level reflectance, MERSI-II NDVI can show less green vegetation in central China. A relationship between MERSI-II and MODIS NDVI is derived for building the long-term VI data records. For MERSI-II EVI, it is found that the current products from the FY ground processing system have large errors. Compared with the operational MERSI-II EVI, our newly derived products have much better consistency with MODIS, especially for croplands.

REFERENCES

Baret, F., J. G. P. W. Clevers, and M. D. Steven, 1995: The robustness of canopy gap fraction estimates from red and near-infrared reflectances: A comparison of approaches. *Remote Sens. Environ.*, **54**, 141–151, doi: 10.1016/0034-4257(95)00136-O.

Blackburn, G. A., 1998: Quantifying chlorophylls and caroteniods at leaf and canopy scales: An evaluation of some hyperspectral approaches. *Remote Sens. Environ.*, **66**, 273–285, doi: 10.1016/S0034-4257(98)00059-5.

Gutman, G., and A. Ignatov, 1998: The derivation of the green vegetation fraction from NOAA/AVHRR data for use in numerical weather prediction models. *Int. J. Remote Sens.*, **19**, 1533–1543, doi: 10.1080/014311698215333.

Han, X. Z., F. Wang, and Y. Han, 2019: *Fengyun-3D* MERSI true color imagery developed for environmental applications. *J. Meteor. Res.*, **33**, 914–924, doi: 10.1007/s13351-019-9028-7.

Huete, A., C. Justice, and W. Van Leeuwen, 1999: MODIS Vegetation Index (MOD13) Algorithm Theoretical Basis Document. University of Virginia, Charlottesville, VA, 15–61 pp.

Jacquemoud, S., C. Bacour, H. Poilvé, et al., 2000: Comparison of four radiative transfer models to simulate plant canopies reflectance: Direct and inverse mode. *Remote Sens. Environ.*, **74**, 471–481, doi: 10.1016/S0034-4257(00)00139-5.

Myneni, R. B., C. D. Keeling, C. J. Tucker, et al., 1997a: Increased plant growth in the northern high latitudes from 1981 to 1991. *Nature*, **386**, 698–702, doi: 10.1038/386698a0.

Myneni, R. B., R. Ramakrishna, R. Nemani, et al., 1997b: Estimation of global leaf area index and absorbed PAR using radiative transfer models. *IEEE Trans. Geosci. Remote Sens.*, **35**, 1380–1393, doi: 10.1109/36.649788.

Rouse, J. W., R. H. Haas, J. A. Schell, et al., 1973: Monitoring vegetation systems in the Great Plains with ERTS. Third ERTS Symposium, NASA SP-351 I, 309–317 pp.

Saunders, R. W., and K. T. Kriebel, 1988: An improved method for detecting clear sky and cloudy radiances from AVHRR data. *Int. J. Remote Sens.*, **9**, 123–150, doi: 10.1080/01431168808954841.

Sims, D. A., A. F. Rahman, V. D. Cordova, et al., 2006: On the use of MODIS EVI to assess gross primary productivity of North American ecosystems. *J. Geophys. Res. Biogeo.*, **111**, G04015, doi: 10.1029/2006JG000162.

Stroppiana, D., S. Pinnock, and J. M. Gregoire, 2000: The global fire product: Daily fire occurrence from April 1992 to December 1993 derived from NOAA AVHRR data. *Int. J. Remote Sens.*, **21**, 1279–1288, doi: 10.1080/014311600210173.

Vermote, E. F., D. Tanré, J. L. Deuzé, et al., 1997: Second simulation of the satellite signal in the solar spectrum, 6S: An overview. *IEEE Trans. Geosci. Remote Sens.*, **35**, 675–686, doi: 10.1109/36.581987.

Wang, J., X. G. Xu, S. G. Ding, et al., 2014: A numerical testbed for remote sensing of aerosols, and its demonstration for evaluating retrieval synergy from a geostationary satellite constellation of GEO-CAPE and GOES-R. *J. Quant. Spectrosc. Radiat. Transfer*, **146**, 510–528, doi: 10.1016/j.jqsrt.2014.03.020.

Waterman, P. C., 1965: Matrix formulation of electromagnetic scattering. *Proc. IEEE*, **53**, 805–812, doi: 10.1109/PROC.1965.4058.

Xu, N., X. H. Niu, X. Q. Hu, et al., 2018: Prelaunch calibration and radiometric performance of the advanced MERSI Ⅱ on FengYun-3D. *IEEE Trans. Geosci. Remote Sens.*, **56**, 4866–4875, doi: 10.1109/TGRS.2018.2841827.

Zeng, X. B., R. E. Dickinson, A. Walker, et al., 2000: Derivation and evaluation of global 1-km fractional vegetation cover data for land modeling. *J. Appl. Meteor.*, **39**, 826–839, doi: 10.1175/1520-0450(2000)039<0826:DAEOGK>2.0.CO;2.

Tech & Copy Editor: Zhirong CHEN